Chapter 6 Water Ice Clouds over the Martian Tropics during Northern Summer

6.1 Introduction

On Mars, water ice clouds both reflect incoming solar radiation and also absorb and re-emit thermal infrared radiation upwelling from the surface in a thin, infrared-transparent atmosphere. Thus, they likely affect the energy budget of both the atmosphere and the surface significantly [*Hinson and Wilson*, 2004; *Wilson et al.*, 2007] and therefore may have a substantial effect on the thermal structure.

Wilson et al. [2008] find significant discrepancies between temperatures in early northern summer simulated by a control run of the UK Mars general circulation model (MGCM) and by a model run assimilating retrievals of temperature and dust column opacity from the Thermal Emission Spectrometer (TES) on Mars Global Surveyor (MGS). *Wilson et al.* [2008] attribute this discrepancy to the radiative effects of water ice clouds, which were not included in the UK MGCM simulations, and find that simulating clouds in the GFDL MGCM results in 5-10 K warmer temperatures in the tropics (in the vicinity of the clouds with the highest water ice mass mixing ratio) and up to 20 K warmer temperatures at 10 Pa at 60° S. Thus, water ice clouds may have both a direct effect on the atmospheric thermal structure through radiative heating/cooling and an indirect effect through dynamical processes.

Observations show that water ice clouds are a common feature in the martian atmosphere. The most optically thick of these clouds are observed on the edge of the winter polar caps and over high volcanoes throughout much of the year and in the tropics

during northern spring and summer [e.g., *Wang and Ingersoll*, 2002; *Smith*, 2004]. While column opacity measurements are useful for constraining the effect of water ice clouds on the surface energy budget, vertical profiling is necessary to constrain their radiative heating/cooling, since the same column opacity could be due to either a shallow ground fog or a vertically extended haze, but the radiative heating rate profiles and dynamical effects in these two cases may be very different.

Retrievals from limb observations by the Mars Climate Sounder (MCS) on Mars Reconnaissance Orbiter (MRO) now provide a rich dataset for exploring the vertical distribution of water ice clouds [*McCleese et al.*, 2007; *Kleinböhl et al.*, 2009]. They already have been used to study south polar hood clouds (Benson et al., 2009, submitted to *J. Geophys. Res.*) and the effects of the thermal tides on clouds [*Lee et al.*, 2009]. Here we use MCS retrievals to investigate the spatial distribution of water ice clouds during northern summer and early northern fall, a period of transition in visible imagery from widespread tropical cloudiness (during the period simulated by *Wilson et al.* [2008]) to the tropics being relatively clear of water ice clouds [*Wang and Ingersoll*, 2002].

6.2 Data and Methods

Atmospheric retrievals from MCS observations provide vertical profiles of pressure, p, (Pa), temperature, T, (K), water ice opacity, i.e., fractional extinction due to water ice per unit height, $d_z\tau$, (km^{-1}) at 842 cm^{-1}, and dust opacity (km^{-1}) at 463 cm^{-1}. *Kleinböhl et al.* [2009] describes the retrieval algorithm and evaluates its success under different observational conditions. For $d_z\tau > 10^{-5}$ km^{-1}, the estimated uncertainty in $d_z\tau$ is typically

~5%. The retrievals analyzed here use an advanced version of the retrieval algorithm that includes a simple scattering approximation in the radiative transfer.

If the effective radius (r_{eff}) and extinction coefficient (Q_{ext}) of the particle size distribution and the density of water ice (ρ_{ice}) are known, the mass mixing ratio of water ice (q_{ice}) can be derived from any individual retrieval (spherical particles are assumed in this case): $q_{ice} = \frac{4}{3}\frac{\rho_{ice}}{Q_{ext}}\frac{d_z\tau}{\rho}r_{eff}$ (6.1)

where ρ is the atmospheric density. I assume ρ_{ice}=900 kg m^{-3} and use the same assumptions for r_{eff} (1.41 μm) and Q_{ext} (0.773) as in the retrieval algorithm. While such a construction is useful for comparison with model output and so will be adopted for the data analysis, it depends on a variety of unwieldy assumptions. For instance, if the grain size of water ice particles is much larger than assumed, r_{eff}/Q_{ext} (and q_{ice}) could increase by a factor of 2. If water ice particles nucleate around dust particles, ρ_{ice} will depend on the thickness of the water ice layer coating the dust particle.

Somewhat more directly, the infrared heating rate due to water ice in the optically thin case is for emission of the surface at temperature T_s and re-emission by the cloud at T_{e}:

$$\frac{dT}{dt} = \beta\frac{\sigma(T_s^4 - T_e^4)}{c_p}\frac{d_z\tau}{\rho} \quad (6.2)$$

where β is a parameter that incorporates variations in the spectral properties of emission, absorption, and scattering of both the surface and the cloud with temperature and wavelength; σ is the Stefan-Boltzmann constant, and c_{p} is the heat capacity of the

atmosphere. Thus, the heating rate is proportional to the density-scaled opacity, $\frac{d_z \tau}{\rho}$, which can be directly calculated from the retrievals, is proportional to q_{ice} as we calculate it, and is affected by the uncertainty in the properties of water ice (and dust) only to the extent that uncertainty affects relative attribution of opacity to dust and water ice in the retrieval algorithm.

For zonal averaging, the retrievals are separated into "dayside" (9:00—21:00 LST) and "nightside" (21:00—9:00 LST) bins and further binned in 36 (5° resolution) mean latitudinal bins, 64 (5.625° resolution) mean longitudinal bins, and L_s bins at 5° resolution: a resolution comparable to Mars general circulation model grids. Away from the poles, MCS normally observes ~3:00 and ~15:00 LST. Mean latitude and longitude refer to the coordinates at the tangent point observed by the center of the MCS detector array at ~40 km above the surface. Opacity at pressures lower than the lowest pressure at which opacity is reported is set to 0 to minimize the impact on the zonal average of rare hazes detached from the bulk of the cloud.

6.3 Results

Figures 6.1a-h show nightside zonal average temperature (K) and q_{ice} for selected L_s bins during northern summer and fall of Mars Year (MY) 29 (2008—2009) (by the convention of *Clancy et al.* [2000]). (The latitude/longitude bins that contribute to the zonal averages in Figure 6.1 are mapped in Figure 6.2). Sampling of longitudinal bins is good in early summer and degrades as the summer progresses. I focus on nightside profiles, because sampling is usually better during the night.

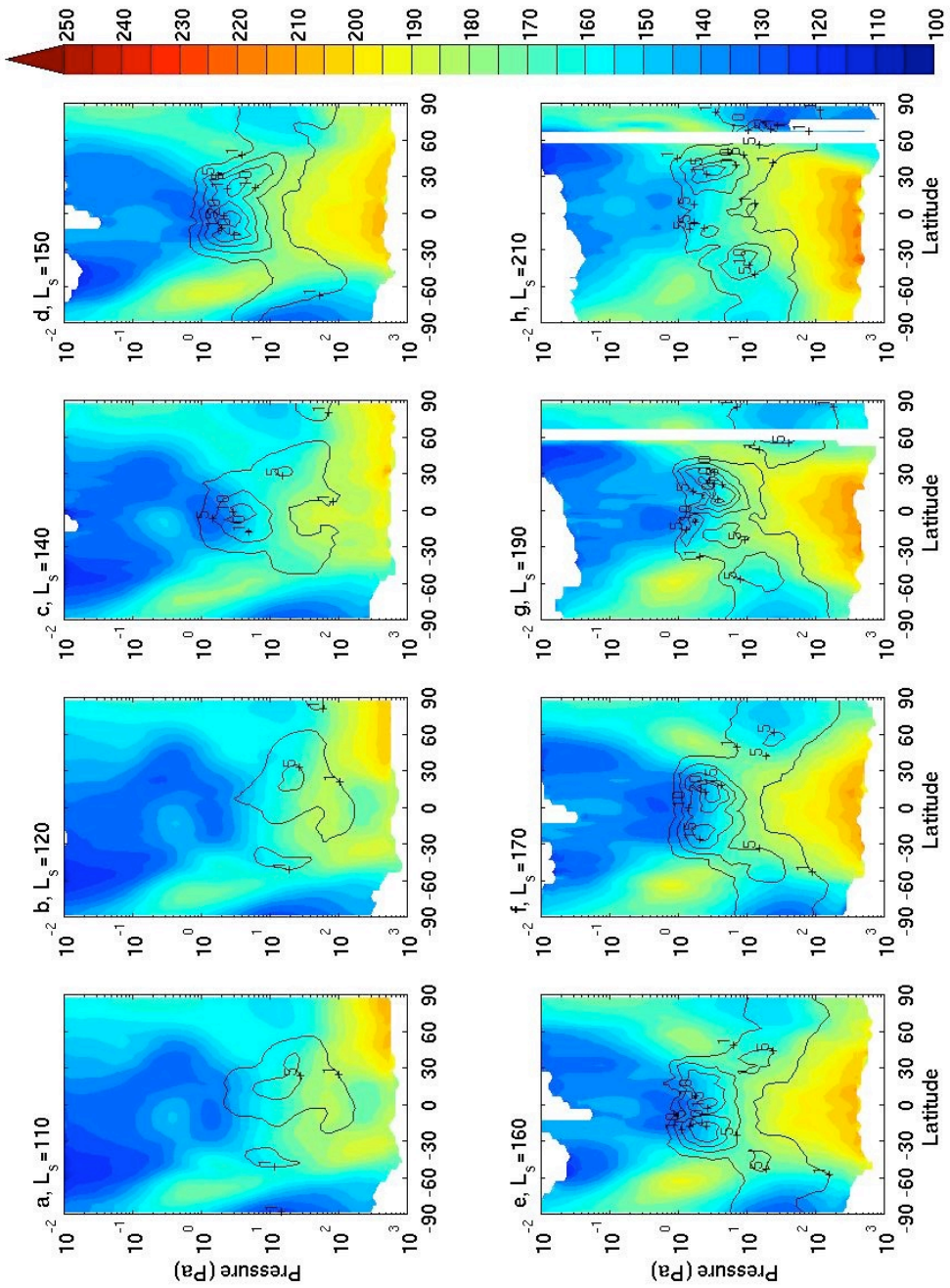

Figure 6.1. Nightside zonal average temperature (K) (color contours) and q_{ice} (ppm) (labeled contours) for selected L_s bins during MY 29 indicated by the labels at the top of each panel.

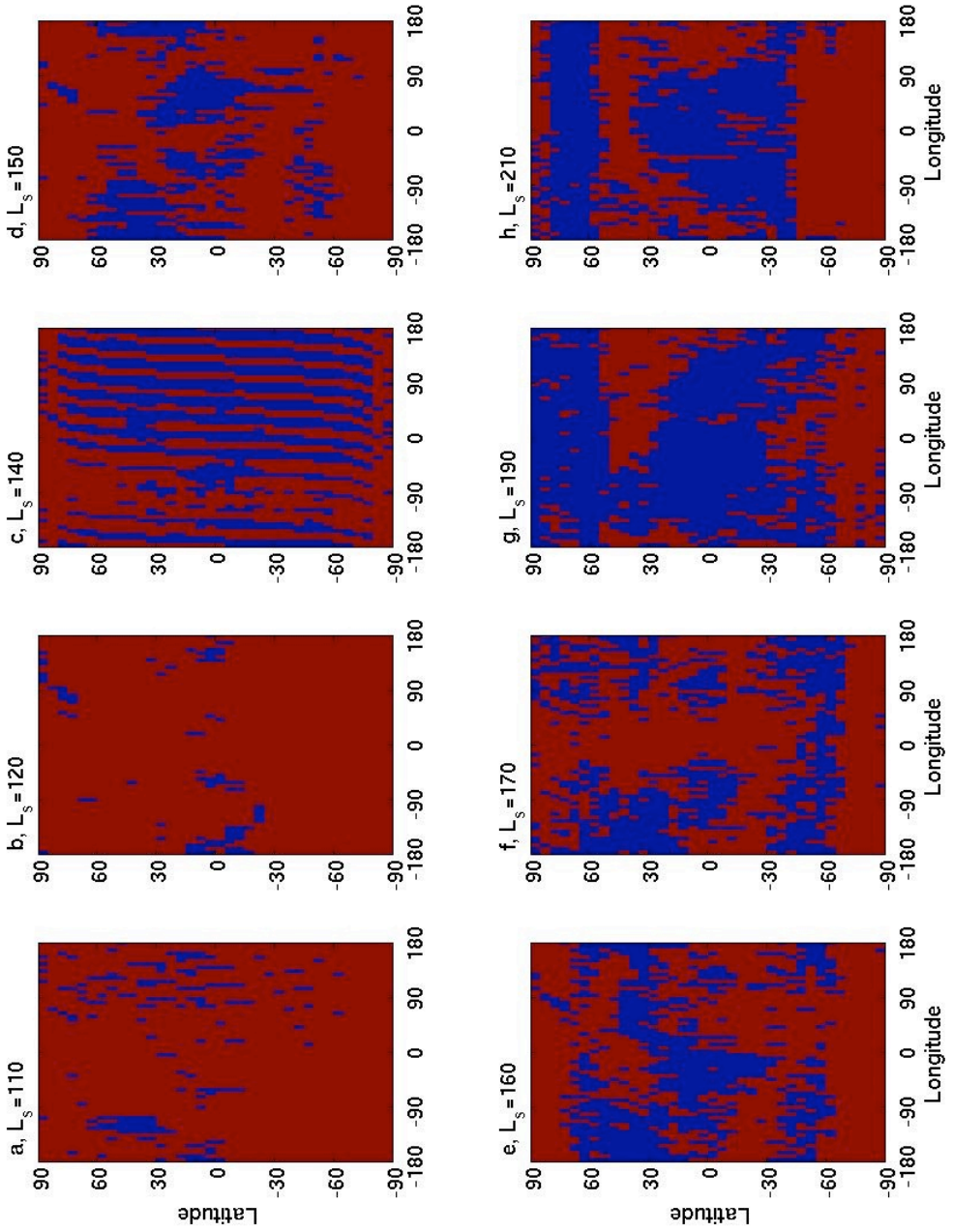

Figure 6.2. Map of latitude/longitude bins with at least one retrieval (red) for the L_s bins (used in Figure 6.1) indicated by the labels on the top of each panel.

In early summer, the highest zonal average nightside q_{ice} is 5 ppm over the northern tropics at ~20 Pa (Figures 6.1a-b). By L_s=140°, a layer of higher q_{ice} (up to 20 ppm) stretches across the tropics at ~4 Pa (Figure 6.1c), and this layer increases in q_{ice} throughout late summer as secondary maxima in q_{ice} of 5 ppm become apparent near 45° N and S at ~10-20 Pa (Figures 6.1e-f). The layer of high q_{ice} at ~4 Pa over the tropics begins to dissipate in early northern fall. Figures 6.3a-d show a similar transition in the distribution of water ice at night during the course of the summer of MY 28, during which longitudinal sampling is somewhat better later in the summer than during MY 29 (Figures 6.4a-d). On the dayside, a tropically symmetric layer of water ice with q_{ice}=5—15 ppm is observed at ~20 Pa throughout northern summer (Figures 6.3e-h), though sampling is very poor (Figures 6.4e-h).

Figures 6.5a-b show longitudinal cross-sections of q_{ice} from a narrow latitude band roughly centered on the northern tropic and intersecting Lycus Sulci and the Elysium Montes. In the example from early summer of MY 29 (Figure 6.5a), there is a layer of high q_{ice} at ~20 Pa, which not vary much in q_{ice} or pressure level with longitude, even at longitudes that cross significant topography. This layer is vertically resolved by the retrievals. In the example from late summer of MY 28 (Figure 6.5b), q_{ice} is more longitudinally variable. There are layers of water ice with similar values of q_{ice} and at similar pressure levels as those in early summer, but there is also a layer at ~3 Pa with q_{ice} up to 65 ppm.

Figures 6.6a-b show longitudinal cross-sections of q_{ice} from a narrow latitude band at the equator that intersects the Tharsis Montes. In the example from early summer

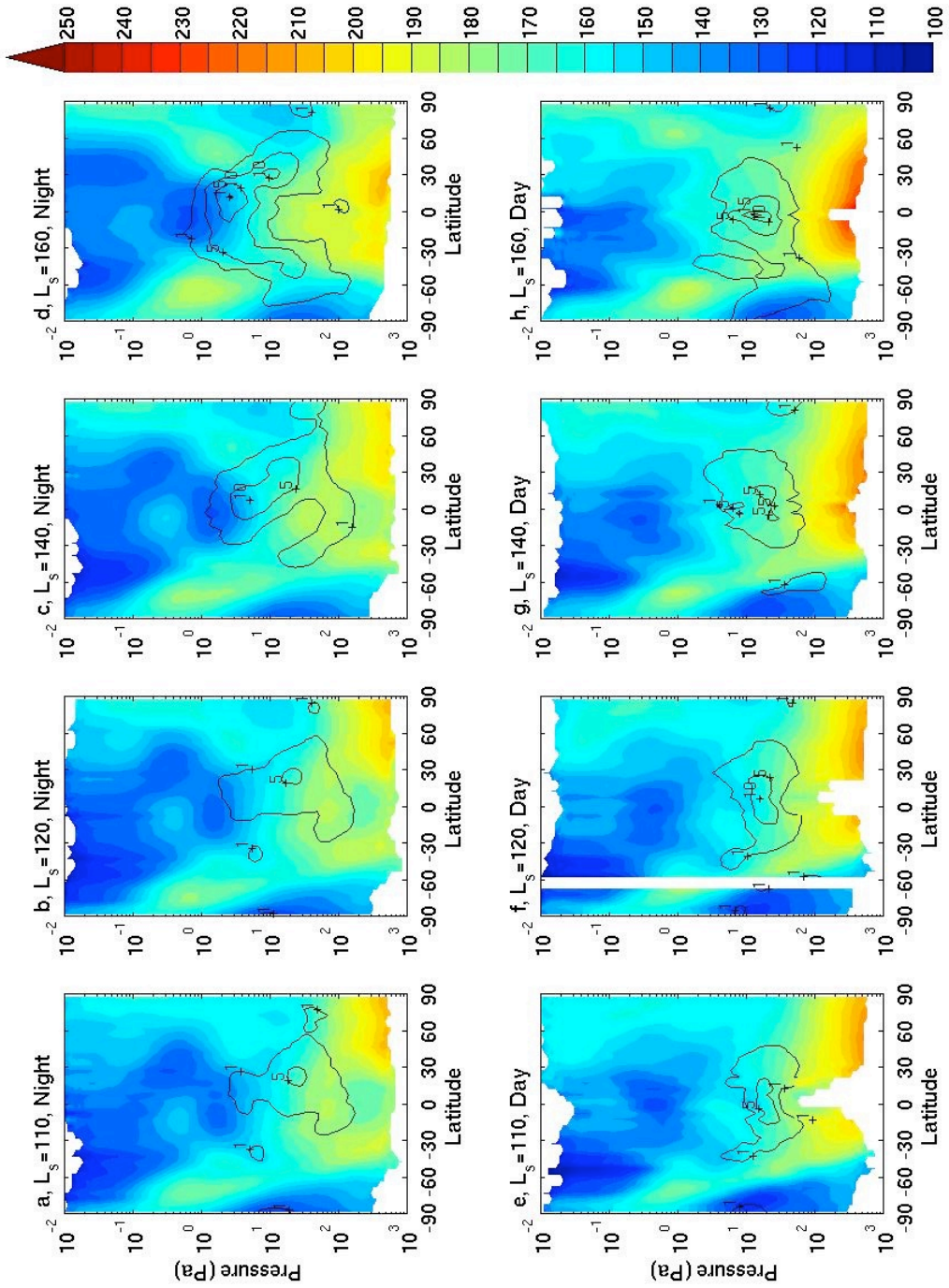

Figure 6.3. Zonal average temperature (K) (color contours) and q_{ice} (ppm) (labeled contours) for selected L_s bins during MY 28 for dayside or nightside as indicated by the labels at the top of each panel.

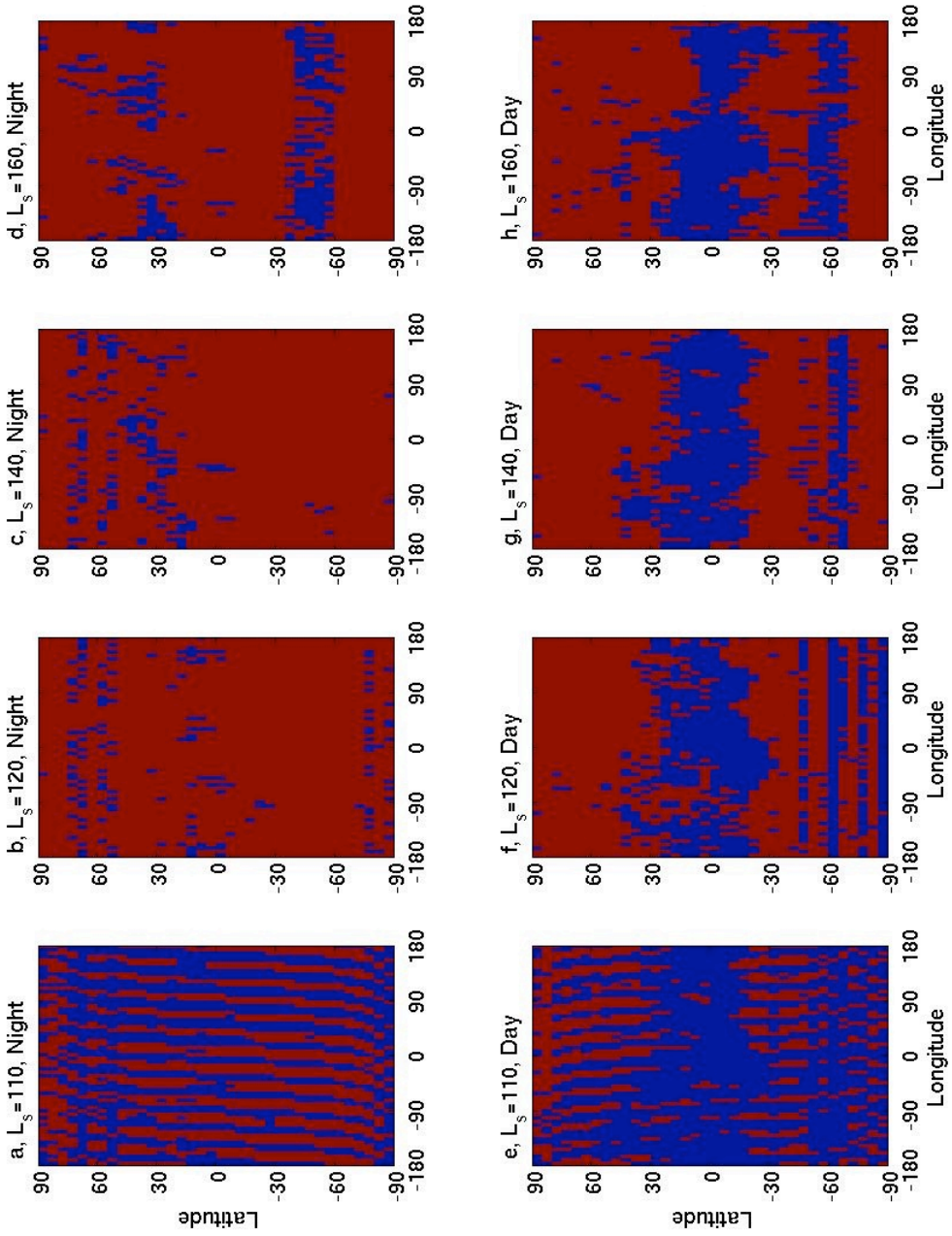

Figure 6.4. Map of latitude/longitude bins with at least one retrieval (red) for the L_s bins (used in Figure 6.3) indicated by the labels on the top of each panel.

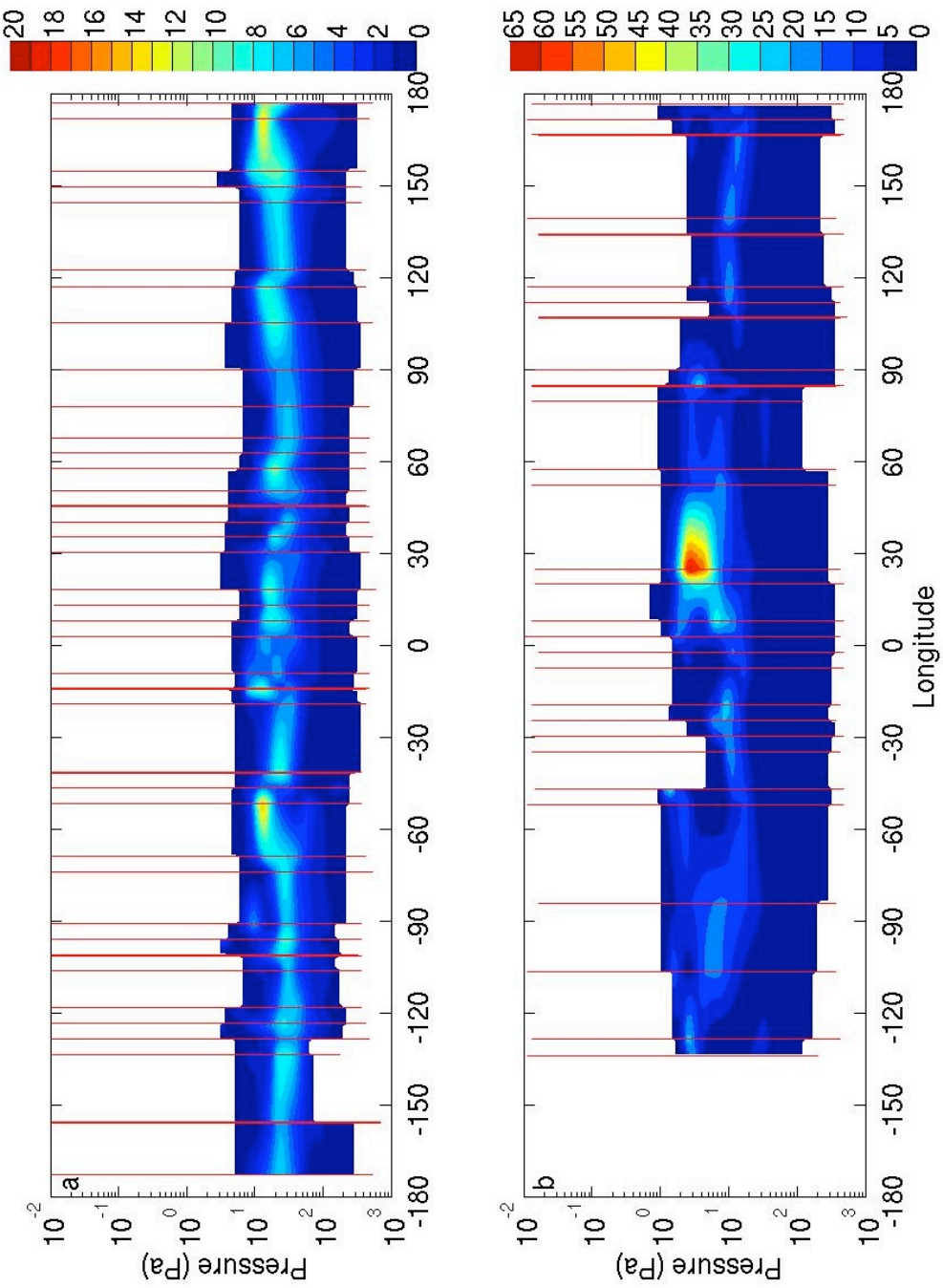

Figure 6.5. q_{ice} (ppm) for two longitudinal cross-sections interpolating retrievals from a narrow range of L_s and latitude: (a) L_s=119°—121°, 24°—26° N, nightside, MY 29; (b) L_s=159°—161°, 24°—26° N, nightside, MY 28. The red lines mark the mean longitude and vertical extent of each retrieval in the cross-section.

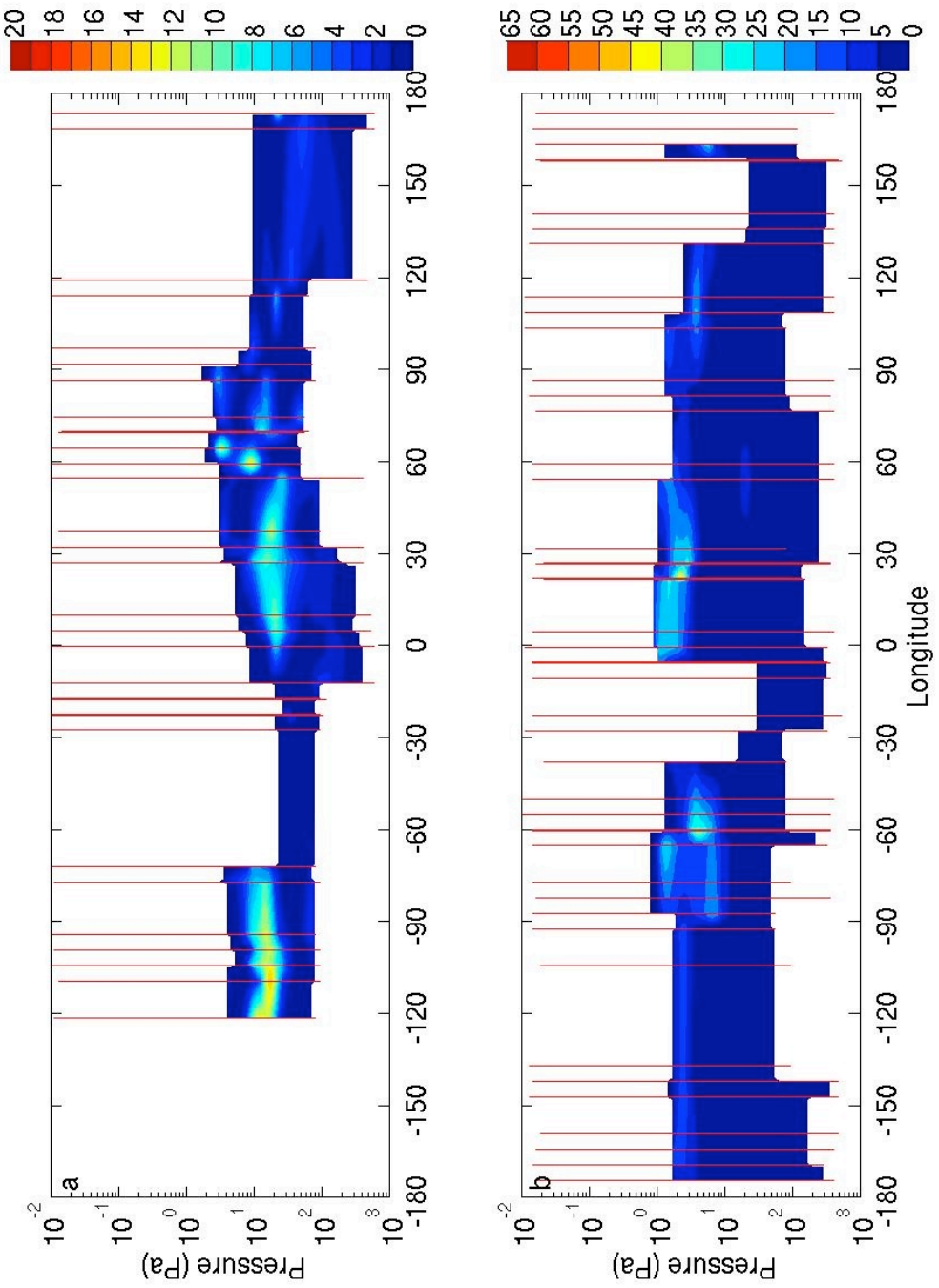

Figure 6.6. q_{ice} (ppm) for two longitudinal cross-sections interpolating retrievals from a narrow range of L_s and latitude: (a) L_s=119°—121°, 1° S—1° N, nightside, MY 29; (b) L_s=159°—161°, 1° S—1° N, nightside, MY 28. The red lines mark the mean longitude and vertical extent of each retrieval in the cross-section.

of MY 29 (Figure 6.4a), there are a couple of vertically resolved layers of $q_{ice} \approx$10 ppm at ~20 Pa. One layer is near and just east of the Tharsis Montes between 120° and 80° W, while the other is between 0° and 60° E. The longitudinal sampling is not as complete as in Figure 6.5a, but the thick water ice clouds seem somewhat more scattered. In the example from late summer, scattered cloudiness is now at a pressure level between 2 and 10 Pa, while the q_{ice} of the thickest layers has increased by around a factor of two.

6.4 Discussion

The tropical water ice distribution in early northern summer and the course of its evolution during northern summer do not appear to be captured well by published models. *Richardson et al.* [2002], *Montmessin et al.* [2004], *Wilson et al.* [2008], and *Nelli et al.* [2009] all predict that the thickest clouds in early summer are mostly in the northern tropics at ~100—300 Pa, a significantly lower level in the atmosphere than where they are observed. (The first three studies present diurnal averages, while *Nelli et al.* [2009] present longitudinal cross-sections for night.) The simulated q_{ice} for these clouds in these published models is ~5 times higher than observed, a discrepancy too great to be explain by an error in the grain size assumption used in Eq 6.1. *Richardson et al.* [2002] does simulate a transition in the tropical water ice distribution during northern summer, but this transition is from a tropically symmetric layer at a pressure level of ~200 Pa at L_s=110° to a thinner layer mainly over the northern tropics at a pressure level of ~100 Pa at L_s=150°. Both of these layers are much lower than observed.

Part of the discrepancy in the pressure level of clouds may be due to the limited vertical range of the retrievals, which is dependent on altitude above the surface rather than pressure. Retrieval near the surface is inhibited by potentially large opacity in the instrument line-of-sight and substantial contributions of emission from the surface in the measured radiances, so the retrievals generally are cut off below ~5—15 km. Thus, the retrieved profiles will miss clouds near the surface, especially in the vicinity of topography, that could contribute high q_{ice} to model simulations at some pressure levels. In Figure 6.6a, for instance, the retrievals near the Tharsis Montes stop at ~80 Pa. This bias is likely intrinsic to limb observations in the thermal infrared at this season. These results agree well with TES limb retrieval results presented by McConnochie and Smith (Vertically Resolved Water Ice Aerosols Opacity From Mars Global Surveyor Thermal Emission Spectrometer (TES) Limb Sounding, Mars Water Cycle Workshop, 21—23 April 2008, Paris, France). But the vertical range bias cannot explain the entirety of the difference between the models and the observed water ice distribution. The vertical range of the retrievals reaches pressures as high as 300 Pa over most of the planet along the northern tropic (Figure 6.5a). Based on the simulations of *Wilson et al.* [2008], we would expect resolve a layer of cloud with q_{ice} 10—20 ppm centered at 100 Pa, but such a layer is not observed.

Lee et al. [2009] argues that the water ice distribution is controlled by the thermal tides. Water vapor is well-mixed to considerable depth in the atmosphere, and water ice condenses if the air temperature is below the saturation vapor pressure of water with respect to ice (and sufficient nuclei are available). Figures 6.5d and 6.5h very clearly support this hypothesis, since the tropical water ice layer on the dayside (nightside) is at a

level of the atmosphere that is warmer (cooler) in the night (day). Thus, a layer of high q_{ice} moves up and down with the thermal tide during late summer.

Eqs. 6.1 and 6.2 permit calculation of the infrared heating due to such a layer. The assumptions are: T_s=263 K (day) and 197 K (night) [*Schofield et al.*, 1997]; T_e=165 K (day) and 145 K (night); β=1 (assumes infrared absorption equivalent to the value at ~12 μ); and c_p=756 J kg^{-1}. In this case, the daytime heating rate is 11.1 K sol^{-1} ppm^{-1} and the nighttime heating rate is 2.9 K sol^{-1} ppm^{-1}. The zonal average diabatic heating/cooling due to CO_2 at northern summer solstice was estimated to range from -20 to 10 K sol^{-1} in a GCM simulation without aerosol by *Medvedev and Hartogh* [2007], so a zonal average of 10—20 ppm water ice cloud in the tropics should produce significant diabatic heating and perturb the circulation. In addition, the heating due to the high q_{ice}, longitudinally scattered clouds in Figure 6.53b and Figures 6.6a-b could be a significant asymmetric forcing.

The most significant difference between the water ice cloud observations presented here and published model results is the level at which water ice clouds are found. *Rind and Rossow* [1984] observes that circulations are perturbed toward a thermally direct state at a given pressure level if the equator to pole temperature gradient is positive. Thus, neglecting eddy terms, radiative heating by water ice may drive a thermally direct circulation like the Hadley cell on the Earth that effectively becomes part of the equivalent to the Hadley cell on Mars: the principal meridional overturning cell (PMOC). The higher the clouds, the deeper the cell. Therefore, the PMOC during northern summer may be stronger at higher altitudes than simulated by both the published models that simulate water ice clouds and by models that do not simulate such clouds.

Since the upwelling of the PMOC controls the tropical water vapor distribution [*Richardson et al.*, 2002; *Richardson and Wilson*, 2002], water ice clouds also could have a positive feedback (mainly limited by the water vapor supply) on the PMOC's height and intensity.

Bibliography

Clancy, R. T., B. J. Sandor, M. J. Wolff, P. R. Christensen, M. D. Smith, J. C. Pearl, B. J. Conrath, and R. J. Wilson (2000), An intercomparison of ground-based millimeter, MGS TES, and Viking atmospheric temperature measurements: Seasonal and interannual variability of temperatures and dust loading in the global Mars atmosphere, *J. Geophys. Res.*, *105*(E4), 9553–9571.

Hinson, D. P., and R. J. Wilson (2004), Temperature inversions, thermal tides, and water ice clouds in the martian tropics, *J. Geophys. Res., 109*, E01002, doi:10.1029/2003JE002129.

Kleinböhl, A., J. T. Schofield, D. M. Kass, W. A. Abdou, C. R. Backus, B. Sen, J. H. Shirley, W. G. Lawson, M. I. Richardson, F. W. Taylor, N. A. Teanby, and D. J. McCleese (2009), Mars Climate Sounder limb profile retrieval of atmospheric temperature, pressure, dust, and water ice opacity, *J. Geophys. Res.*, *114*, E10006, doi: 10.1029/2009JE003358.

Lee, C., W.G. Lawson, M.I. Richardson, N.G. Heavens, A. Kleinböhl, D. Banfield, D.J. McCleese, R. Zurek, D. Kass, J.T. Schofield, C.B. Leovy, F.W. Taylor, A.D. Toigo, (2009), Thermal tides in the martian middle atmosphere as seen by the Mars Climate Sounder, *J. Geophys. Res.*, *114*, E03005, doi:10.1029/2008JE003285.

McCleese, D. J., J. T. Schofield, F. W. Taylor, S. B. Calcutt, M. C. Foote, D. M. Kass, C. B. Leovy, D. A. Paige, P. L. Read, and R. W. Zurek (2007), Mars Climate Sounder: An

investigation of thermal and water vapor structure, dust and condensate distributions in the atmosphere, and energy balance of the polar regions, *J. Geophys. Res.*, *112*, E05S06, doi:10.1029/2006JE002790.

Medvedev, A.S. and P. Hartogh (2007), Winter polar warmings and the meridional transport on Mars simulated with a general circulation model, *Icarus*, *186*(1), 97-110.

Montmessin, F., F. Forget, P. Rannou, M. Cabane, and R. M. Haberle (2004), Origin and role of water ice clouds in the martian water cycle as inferred from a general circulation model, *J. Geophys. Res.*, *109*, E10004, doi:10.1029/2004JE002284.

Nelli, S. M., J. R. Murphy, W. C. Feldman, and J. R. Schaeffer (2009), Characterization of the nighttime low-latitude water ice deposits in the NASA Ames Mars General Circulation Model 2.1 under present-day atmospheric conditions, *J. Geophys. Res.*, *114*, E11003, doi:10.1029/2008JE003289.

Richardson, M. I., and R. J. Wilson (2002), Investigation of the nature and stability of the martian seasonal water cycle with a general circulation model, *J. Geophys. Res.*, *107*(E5), 5031, doi:10.1029/2001JE001536.

Richardson, M. I., R. J. Wilson, and A. V. Rodin (2002), Water ice clouds in the martian atmosphere: General circulation model experiments with a simple cloud scheme, *J. Geophys. Res.*, *107*(E9), 5064, doi:10.1029/2001JE001804.

Rind, D., and W.B. Rossow (1984), The effects of physical processes on Hadley circulation, *J. Atmos. Sci.*, *41*, 479-507.

Schofield, J. T., J. R. Barnes, D. Crisp, R. M. Haberle, S. Larsen, J. A. Magalhães, J. R. Murphy, A. Seiff, and G. Wilson (1997), The Mars Pathfinder Atmospheric Structure Investigation/Meteorology (ASI/MET) Experiment, *Science*, *278*, 1752–1758.

Smith, M. D. (2004), Interannual variability in TES atmospheric observations of Mars during 1999– 2003, *Icarus*, *108*, 148– 165.

Wang, H., and A. P. Ingersoll (2002), martian clouds observed by Mars Global Surveyor Mars Orbiter Camera, *J. Geophys. Res.*, 107(E10), 5078, doi:10.1029/2001JE001815.

Wilson, R. J., G. A. Neumann, and M. D. Smith (2007), Diurnal variation and radiative influence of martian water ice clouds, *Geophys. Res. Lett.*, *34*, L02710, doi:10.1029/2006GL027976.

Wilson, R. J., S. R. Lewis, L. Montabone, and M. D. Smith (2008), Influence of water ice clouds on martian tropical atmospheric temperatures, *Geophys. Res. Lett.*, *35*, L07202, doi:10.1029/2007GL032405.